

SPITZER SECONDARY ECLIPSES OF WASP-18b

SARAH NYMEYER¹, JOSEPH HARRINGTON¹, RYAN A. HARDY¹, KEVIN B. STEVENSON¹, CHRISTOPHER J. CAMPO¹,
 NIKKU MADHUSUDHAN², ANDREW COLLIER-CAMERON³, THOMAS J. LOREDO⁴, JASMINA BLECIC¹, WILLIAM C. BOWMAN¹,
 CHRISTOPHER B. T. BRITT¹, PATRICIO CUBILLOS¹, COEL HELLIER⁵, MICHAEL GILLON⁶, PIERRE F. L. MAXTED³,
 LESLIE HEBB⁷, PETER J. WHEATLEY⁸, DON POLLACCO⁹, AND DAVID R. ANDERSON⁵

¹ Planetary Sciences Group, Department of Physics, University of Central Florida, Orlando, FL 32816-2385, USA; sarah.nymeyer@gmail.com

² Department of Astrophysical Sciences, Princeton University, Princeton, NJ 08544, USA

³ School of Physics and Astronomy, University of St. Andrews, North Haugh, Fife KY16 9SS, UK

⁴ Center for Radiophysics and Space Research, Space Sciences Building, Cornell University, Ithaca, NY 14853-6801, USA

⁵ Astrophysics Group, Keele University, Staffordshire ST5 5BG, UK

⁶ Institut d'Astrophysique et de Géophysique, Université de Liège, Allée du 6 Août 17, Bat. B5C, 4000 Liège, Belgium

⁷ Department of Physics and Astronomy, Vanderbilt University, Nashville, TN 37235, USA

⁸ Department of Physics, University of Warwick, Coventry CV4 7AL, UK

⁹ Astrophysics Research Centre, School of Mathematics & Physics, Queen's University, University Road, Belfast BT7 1NN, UK

Received 2010 May 6; accepted 2011 August 15; published 2011 November 3

ABSTRACT

The transiting exoplanet WASP-18b was discovered in 2008 by the Wide Angle Search for Planets project. The *Spitzer* Exoplanet Target of Opportunity Program observed secondary eclipses of WASP-18b using *Spitzer*'s Infrared Array Camera in the 3.6 μm and 5.8 μm bands on 2008 December 20, and in the 4.5 μm and 8.0 μm bands on 2008 December 24. We report eclipse depths of $0.30\% \pm 0.02\%$, $0.39\% \pm 0.02\%$, $0.37\% \pm 0.03\%$, $0.41\% \pm 0.02\%$, and brightness temperatures of 3100 ± 90 , 3310 ± 130 , 3080 ± 140 , and 3120 ± 110 K in order of increasing wavelength. WASP-18b is one of the hottest planets yet discovered—as hot as an M-class star. The planet's pressure–temperature profile most likely features a thermal inversion. The observations also require WASP-18b to have near-zero albedo and almost no redistribution of energy from the day side to the night side of the planet.

Key words: infrared: planetary systems – planets and satellites: atmospheres – planets and satellites: composition – planets and satellites: individual (WASP-18b)

Online-only material: color figures, supplemental data (FITS) file (tar.gz)

1. INTRODUCTION

Among the more than 500 extrasolar planets discovered to date,¹⁰ over 100 close-orbiting gas giants that transit their host stars have provided the most valuable clues to their physical natures. The geometry of the transit gives a direct measurement of the density of the host star and the surface gravity of the planet (Seager & Mallén-Ornelas 2003; Southworth et al. 2007). These measurements can be combined with an estimate of the star's mass and radius to provide estimates of the planet's mass, radius, and density. The closest-orbiting planets attain daytime temperatures high enough to give observable secondary eclipses at thermal-infrared wavelengths as they pass behind their host stars (e.g., Charbonneau et al. 2005; Deming et al. 2005; Sing & López-Morales 2009).

Observations with the *Spitzer Space Telescope* have revealed that transiting gas giant planets can be divided into two classes based on their infrared spectral energy distributions. A subset of the very hottest planets, with dayside temperatures in excess of 2000 K, displays molecular features of CO and H₂O in emission rather than absorption, indicating the presence of a temperature increase with height in the planet's photospheric layers. Such temperature inversions have been inferred from the flux ratios between the four bandpasses of the Infrared Array Camera (IRAC; Fazio et al. 2004) on board *Spitzer*, centered at 3.6, 4.5, 5.8, and 8.0 μm (channels 1–4), in the hot planets HD209458b (Burrows et al. 2008; Knutson et al. 2008), XO-1b (Machalek et al. 2008), TrES-2b (O'Donovan et al. 2010),

TrES-4b (Knutson et al. 2009a), XO-2b (Machalek et al. 2009), and WASP-1b (Wheatley et al. 2011), among others. This phenomenon has been attributed to the presence of strongly absorbing species such as TiO and VO remaining in the gas phase in the upper atmosphere, leading to the formation of a stratospheric temperature inversion (Burrows et al. 2008; Fortney et al. 2008). This led Fortney et al. to propose a scheme in which planets are assigned to class pM (with hot stratospheres) or pL (without) according to temperature, analogous to the stellar M and L spectral classes. Knutson et al. (2010) suggest instead that some planets lack inversions because the TiO and VO are destroyed by UV radiation, while Spiegel et al. (2009) claimed that TiO/VO may not be sufficiently abundant in the upper atmospheres to produce the required inversions. Zahnle et al. (2009b) proposed additional absorbers, like sulphur species, which could potentially form thermal inversions.

WASP-18b is a prime candidate for secondary-eclipse observations to test for the presence of a hot stratosphere (Hellier et al. 2009). It orbits an F6-type star with a period of just 0.94 days and is expected to attain a blackbody equilibrium temperature approaching 2400 K, assuming zero albedo and efficient transport of heat from the day side to the night side of the planet. With less efficient transport, an even higher dayside temperature is expected. The planet is unusual because of its very high mass, $M_p = 10.43 \pm 0.30$ Jupiter masses, M_{Jup} , and modest radius, $R_p = 1.165 \pm 0.055$ Jupiter radii, R_{Jup} (Southworth et al. 2009), which give it a surface gravity an order of magnitude greater than that of any known transiting planet likely to belong to the pM class. The pressure scale height in its photospheric layers should

¹⁰ For an up-to-date listing, see <http://www.exoplanet.eu>.

Table 1
Run Parameters

Obs.	Date	λ (μm)		Pre-observation			Main Observation			Post-observation		
				Start ^a	Frame Time (s)	Frames	Start ^a	Frame Time (s)	Frames	Start ^a	Frame Time (s)	Frames
CH13	2008 Dec 20	3.6	5.8	820.57796	2, 12	260	820.61869	2, 12	1148	820.79721	2, 12	10
CH24	2008 Dec 24	4.5	8.0	824.35796	12	185	824.38431	2, 12	1148	824.56278	2, 12	10

Note. ^a BJD – 2,454,000 ephemeris time.

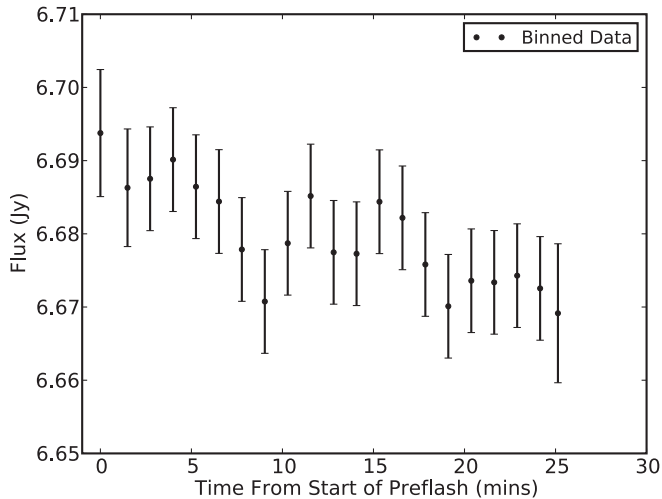


Figure 1. Preflash light curve. These are $8\mu\text{m}$ data, analyzed with aperture photometry. The preflash source is bright compared to WASP-18, which allows the array sensitivity to stabilize before the science observations. Without a preflash, similar observations generally show a steeper and longer ramp in the eclipse observations. This may be the first descending preflash, attributed to an even brighter source in the immediately preceding program.

therefore be an order of magnitude smaller than for planets of similar temperature, providing an important new dimension for tests of planetary atmospheric models in the presence of strong external irradiation. The small but precisely known orbital eccentricity $e = 0.0085 \pm 0.0008$ (Triaud et al. 2010) may impart slightly-faster-than-synchronous rotation, which could help to redistribute heat from the day side to the night side of the planet.

WASP-18b was therefore selected as a candidate for observation as part of our *Spitzer* Exoplanet Target of Opportunity Program shortly after its discovery was confirmed. In Sections 2 and 3, we describe the observations and the analysis of the data. In Section 4, we discuss the constraints imposed on the thermal structure of the planetary atmosphere by the IRAC fluxes, in Section 5 we compare the eccentricity and orientation of the orbit from the timing and duration of the secondary eclipse with the values derived from radial velocity (RV) observations, and in Section 6 we present our conclusions.

2. OBSERVATIONS

Spitzer’s IRAC instrument observed (program 50517) two secondary eclipses (see Table 1). After each observation, an offset six-minute full-array sequence confirmed the lack of persistent bad pixels near the stellar position. There are two independent analyses of these data, one presented here and one by Machalek et al. (2011).

IRAC exhibits some sources of systematic noise that must be taken into account when planning and analyzing observations. A positional sensitivity exists in the 3.6 and $4.5\mu\text{m}$ channels (Charbonneau et al. 2005; Knutson et al. 2009b; Machalek et al. 2011; Stevenson et al. 2010), and a time-varying sensitivity

(“ramp”) exists in the 5.8 and $8.0\mu\text{m}$ channels (Charbonneau et al. 2005; Harrington et al. 2007).

The time-varying sensitivity in the $8.0\mu\text{m}$ channel manifests as an apparent increase in flux with time. The rate of increase depends on the number of photons received by each pixel and is believed to be caused by charge trapping. The effect is successfully reduced by staring at a bright diffuse source, in this instance an H II ionized region, prior to the main observation (a “preflash”). The large number of photons quickly saturates the detector, resulting in a smaller rate of increase in the main observation than is seen without a preflash (Knutson et al. 2009b). We observed a 30 minute preflash prior to the December 24 event (see Figure 1), which exhibits a decreasing ramp, unlike previous observations (Knutson et al. 2009b; Campo et al. 2011). This is attributable to the previous IRAC observation of the bright extended source IC1396a.

The $5.8\mu\text{m}$ channel exhibits a decreasing ramp, so *Spitzer* stared at the target for 62 minutes prior to the observation to allow time for the detector to stabilize. In order to minimize the positional sensitivity at 3.6 and $4.5\mu\text{m}$, each observation used fixed pointing.

3. DATA ANALYSIS

All data are *Spitzer* basic calibrated data frames using version S18.7.0 of *Spitzer*’s preprocessing pipeline. This pipeline removes all well-understood instrumental signatures and produces a flux-calibrated image (Fazio et al. 2004). We first account for light travel time in the solar system by converting to Barycentric Julian Date (BJD), and then mask all pixels in the *Spitzer*-supplied permanently bad pixel mask. We find the remaining bad pixels by grouping sets of 64 frames and doing a two-iteration outlier rejection at each pixel location. Within each array position in each set, this routine calculates the standard deviation from the median, masks any pixels with greater than 4σ deviation, and repeats this procedure once. Masked pixels do not participate in the analysis.

WASP-18 is very bright relative to the background. A two-dimensional Gaussian fit to data within 4 pixels of the stellar brightness peak determines the stellar center in each frame. The light curve comes from five-times-interpolated aperture photometry (Harrington et al. 2007), excluding frames with masked pixels in the photometry aperture and not using masked pixels in sky level averages. Table 2 presents photometry parameters. We vary the aperture radius between 2.0 and 5.0 pixels in 0.25 pixel increments, choosing the one with the best light curve fit as described below.

We model the intrapixel variation affecting the 3.6 and $4.5\mu\text{m}$ channels with a second-order, two-dimensional polynomial (Knutson et al. 2008; Stevenson et al. 2010; Campo et al. 2011),

$$V_{\text{IP}}(x, y) = p_1 y^2 + p_2 x^2 + p_3 xy + p_4 y + p_5 x + 1, \quad (1)$$

where x and y are the centroid coordinates relative to the pixel center nearest the median position, and p_1 – p_5 are free

Table 2
Details of the Analysis and Results from Light-curve Fit

Parameter	3.6 μm	4.5 μm	5.8 μm	8.0 μm
Array position (\bar{x} , pixels)	30.24	23.20	24.41	24.17
Array position (\bar{y} , pixels)	23.89	24.68	24.05	22.32
Position consistency ^a (δ_x , pixels)	0.018	0.019	0.028	0.022
Position consistency ^a (δ_y , pixels)	0.018	0.038	0.015	0.021
Aperture size (pixels)	3.50	3.00	3.75	3.50
Sky annulus inner radius (pixels)	7	7	7	7
Sky annulus outer radius (pixels)	12	12	12	12
System flux (F_s , μJy)	168080 \pm 140	104300 \pm 600	69690 \pm 20	37450 \pm 10
Eclipse depth (F_p/F_s , %)	0.30 \pm 0.02	0.39 \pm 0.02	0.37 \pm 0.03	0.41 \pm 0.02
Brightness temperature (K)	3100 \pm 90	3310 \pm 130	3080 \pm 140	3120 \pm 110
Eclipse mid-time (t_{mid} , phase) ^b	0.4995 \pm 0.0007	0.4985 \pm 0.0006	0.4995 \pm 0.0007	0.4985 \pm 0.0006
Eclipse mid-time (t_{mid} , BJD $-2,454,000$) ^b	820.7160 \pm 0.0006	824.4809 \pm 0.0005	820.7160 \pm 0.0006	824.4809 \pm 0.0005
Eclipse duration (t_{4-1} , s) ^b	8010 \pm 60	8010 \pm 60	8010 \pm 60	8010 \pm 60
Ingress (t_{2-1}) and egress (t_{4-3}) times (s) ^b	857	857	857	857
Ramp name	Linear	Linear	Falling exponential	Rising exponential
Ramp, linear term (r_1)	0.005 \pm 0.001	-0.006 ± 0.003	0	0
Ramp, curvature (r_2)	0	0	14 \pm 1	17 \pm 1
Ramp, time offset (r_3)	0	0	-0.035689	0.082618
Intrapixel, quadratic term in x (p_2)	0	0.47 \pm 0.13	0	0
Intrapixel, cross term (p_3)	0	-0.12 ± 0.01	0	0
Intrapixel, linear term in y (p_4)	0.067 \pm 0.004	0	0	0
Intrapixel, linear term in x (p_5)	-0.086 ± 0.003	-0.33 ± 0.06	0	0
Total frames	1148	1148	1148	1148
Good frames	1142	987	996	1031
Rejected frames (%)	0	14	13	10
Standard deviation of normalized residuals	0.002428	0.003485	0.003738	0.002928
Uncertainty scaling factor	0.31674	0.47164	0.57274	0.47792

Notes.

^a rms frame-to-frame position difference.

^b Duration and ingress/egress time are each a single parameter shared among all four wavelengths. Eclipse mid-times are a single parameter for each pair of channels observed together.

parameters. The systematics had little to no dependence on the quadratic y term, so p_1 is fixed to zero for all models. The ramps for the 3.6 and 4.5 μm channels use a linear model,

$$R(t) = r_1(t - 0.5) + 1, \quad (2)$$

where t is the orbital phase and r_1 is a free parameter. We model the 5.8 μm channel with a falling exponential

$$R(t) = 1 + \exp(-r_2[t - r_3]), \quad (3)$$

and the 8.0 μm channel with a rising exponential (Harrington et al. 2007)

$$R(t) = 1 - \exp(-r_2[t - r_3]), \quad (4)$$

where r_2 and r_3 are free parameters. The r_3 term is fixed to its best-fit value. The eclipse, $E(t)$, is a Mandel & Agol (2002) model, which includes the time of secondary eclipse, t_1 to t_4 duration (1st to 4th contact), ingress/egress time, and eclipse depth.

The single-channel light curve model is

$$F(x, y, t) = F_s V_{\text{IP}}(x, y) R(t) E(t), \quad (5)$$

where $F(x, y, t)$ is the flux measured from interpolated aperture photometry and F_s is the (constant) system flux outside of eclipse, including the planet. We dropped a small number of initial frames in each light curve (0, 150, 100, and 80 frames in order of increasing wavelength) to allow the pointing and

instrument to stabilize. The model lines in Figure 2 show which points are included, as do the electronic light curve files. We fit Equation (5) to the data using a least-squares minimizer. Because the Spitzer pipeline usually overestimates uncertainties, we re-scale the photometric uncertainties to produce a reduced χ^2 of 1 and re-run the fit. This typically converges in one iteration. For a given photometric set the scaling factors are almost identical for all models, so we choose one for use with all models.

Because the underlying physics of the systematics have not been characterized sufficiently to find an expression that fits well in every case, it is possible that, for some *Spitzer* data sets, different investigators will find different values for key parameters when using different systematic models and photometry parameters. This occurred, for example, when Knutson et al. (2009b) re-analyzed the data of Harrington et al. (2007), finding an eclipse about half as deep. The χ^2 minimum that Knutson et al. found was present in the correlation plots of Harrington et al., but it was just a local minimum for that model. While models for deep eclipses, such as those presented here and by Campo et al. (2011), should generally produce compatible results even with different systematic models, weak eclipses such as those of Harrington et al. (2007) and Stevenson et al. (2010) are more dependent on the details of fitting.

All of the published results of our current pipeline (Stevenson et al. 2010; Campo et al. 2011; this work) result from testing a variety of models for each systematic, as well as assessing the best photometry aperture and stabilization time for each data set. We test linear, quadratic, quartic-in-log-time, falling or rising

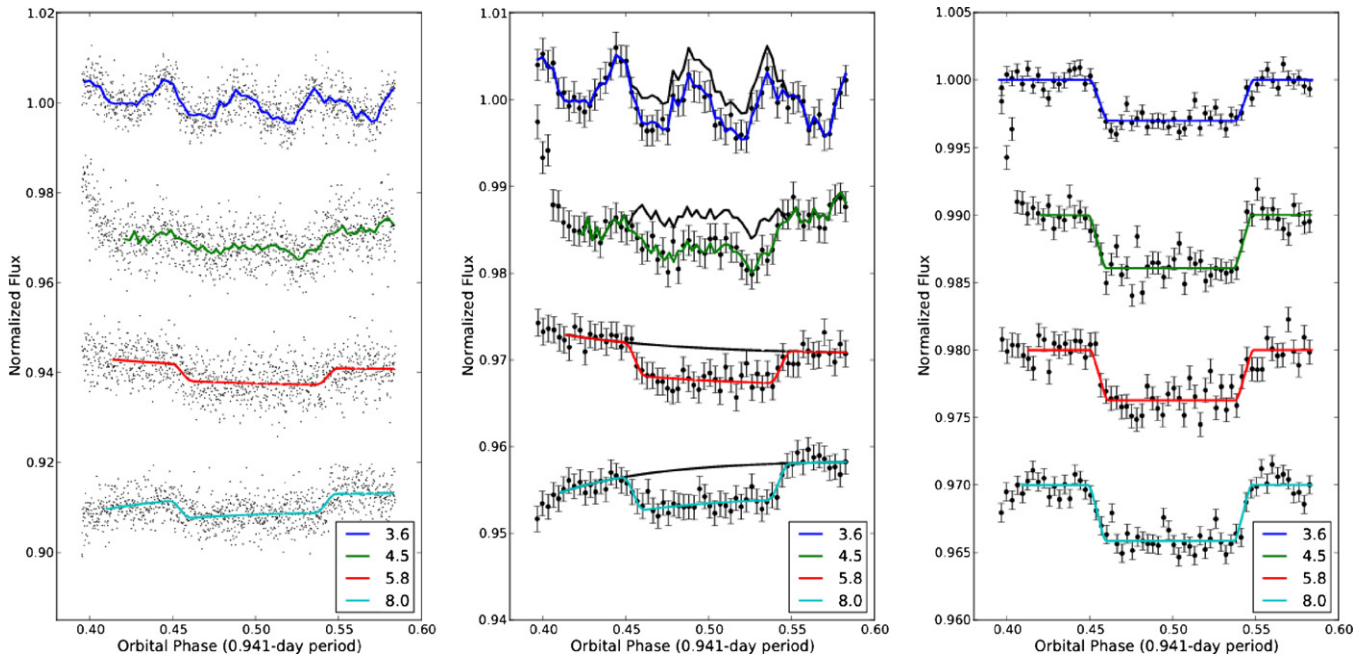


Figure 2. Raw (left), binned (center), and systematics-corrected (right) secondary-eclipse light curves of WASP-18b in the four IRAC channels, normalized to the mean system flux within the fitted data. Colored lines are the best-fit models; black curves omit their eclipse model elements. A few initial points in all channels are not fit, as indicated, to allow the telescope and instrument to stabilize.

(A color version of this figure is available in the online journal.)

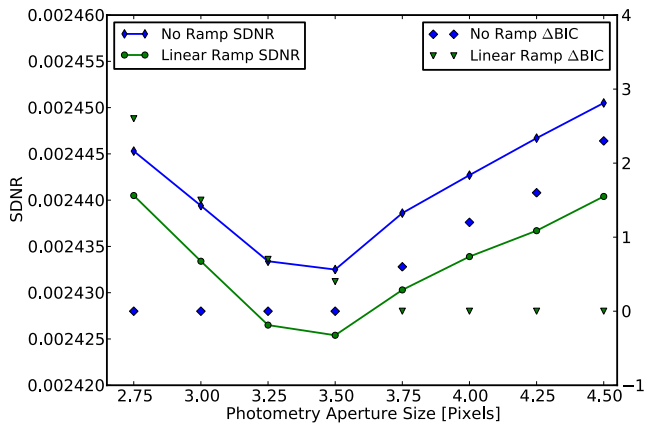


Figure 3. Channel 1. SDNR and ΔBIC vs. aperture size. A lower value indicates a better model fit.

(A color version of this figure is available in the online journal.)

exponential, logarithmic-plus-quadratic, and logarithmic-plus-linear ramps, and a variety of polynomial intrapixel models, before choosing the final models. Most of the possibilities produce obvious bad fits. For this paper we select the best two models in each channel and fit them for all apertures.

For each channel, photometry using the various aperture sizes produces slightly different data sets. We must select first the best data set and then the best model, but χ^2 and related fitting criteria only compare different models to a single data set; they are inappropriate for deciding between models fit to different data sets. For data sets from different apertures, we choose the one with the smallest standard deviation of normalized residuals (SDNR) with respect to the system flux for a given model and repeat for each of several models. This generally results in a consistent choice of the best aperture size among different models.

Once we have the optimal aperture size, we then compare the models. Since adding additional parameters to a model will

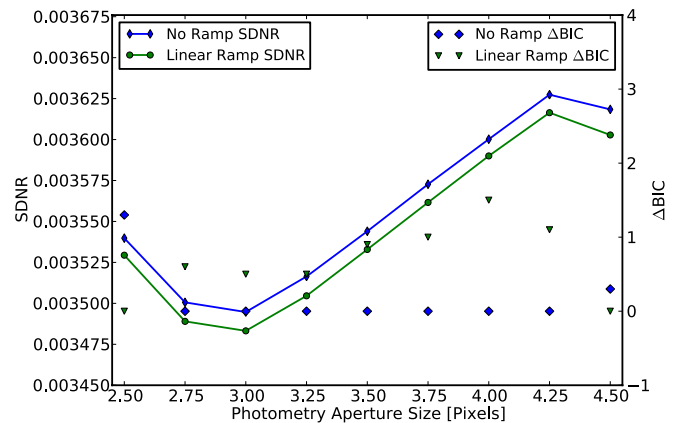


Figure 4. Channel 2. SDNR and ΔBIC vs. aperture size. A lower value indicates a better model fit.

(A color version of this figure is available in the online journal.)

always produce a better fit, we use fitting criteria that properly penalize the addition of parameters. As described by Campo et al. (2011), we apply both the Akaike Information Criterion,

$$\text{AIC} = \chi^2 + 2k, \quad (6)$$

where k is the number of free parameters, and the Bayesian Information Criterion,

$$\text{BIC} = \chi^2 + k \ln N, \quad (7)$$

where N is the number of data points (Liddle 2007). A lower information criterion value indicates a better model. Figures 3–6 present SDNR and BIC with the two main candidate models and aperture sizes for each wavelength. Our final joint model fit, with 28 free parameters, combines the eclipse durations for all channels and pairs the simultaneously observed mid-times. It resulted in an AIC of 4176 and a BIC of 4302.

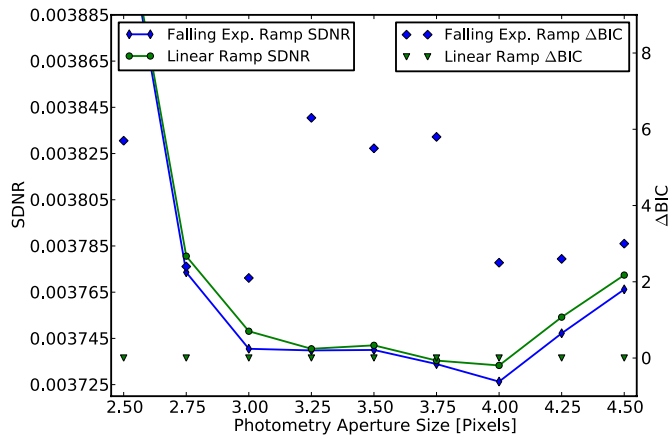


Figure 5. Channel 3. SDNR and ΔBIC vs. aperture size. A lower value indicates a better model fit.

(A color version of this figure is available in the online journal.)

To assess parameter uncertainties and correlations we explore phase space with a Metropolis random-walk Markov Chain Monte Carlo (MCMC) routine. Each chain began at the least-squares minimum. If any step in the chain ever beat the minimum, it would indicate an even deeper minimum at the bottom of the basin of attraction just entered, so the routine would discard the MCMC data, re-run the minimizer, and restart the Markov Chain. The routine runs a “burn-in” of at least 10^5 iterations to forget the starting conditions, and then runs four million iterations.

We also consider the level of correlation in the residuals. For this, we plot rms model residuals versus bin size (Pont et al. 2006; Winn et al. 2008) and compare to the theoretical $1/\sqrt{N}$ rms scaling. Figure 7 demonstrates the lack of significant photometric noise correlation in our final models. In the case of channel 3, we found a high degree of correlation between some of the model parameters in the posterior distribution, and prefer a less-correlated model with insignificantly poorer BIC and similar SDNR at 3.75 rather than 4.0 pixel aperture size. Differences in interesting parameter values for the near-optimal alternative are $\lesssim 1\sigma$.

Finally, the marginal posterior distributions (i.e., the parameter histograms) and plots of their pairwise correlations help in assessing whether the phase space minimum is global and in determining parameter uncertainties. We present these plots for the astrophysical parameters in Figures 8–11. Table 2 gives the values and uncertainties of all parameters.

The data files containing the light curves, best-fit models, centering data, etc., are included in the online journal. Multiple teams analyze the same *Spitzer* exoplanet data, sometimes obtaining divergent results (e.g., Beaulieu et al. 2011; Stevenson et al. 2010; Knutson et al. 2009b; Harrington et al. 2007). To facilitate comparison of these efforts, we encourage all investigators to make a similar disclosure in future reports of exoplanetary transits and eclipses. Because of differing photometry methods and the vagaries of estimating error, the standard deviation of the residuals, normalized to the out-of-eclipse flux, should be the figure of merit for comparing analyses of the same data by different pipelines.

4. ATMOSPHERE

We model WASP-18b with the exoplanet atmospheric modeling and retrieval technique developed by Madhusudhan &

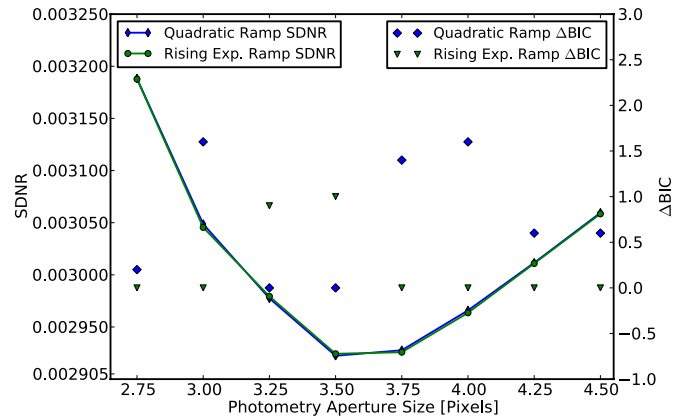


Figure 6. Channel 4. SDNR and ΔBIC vs. aperture size. A lower value indicates a better model fit.

(A color version of this figure is available in the online journal.)

Seager (2009). This is a one-dimensional, line-by-line, radiative-transfer model with constraints of hydrostatic equilibrium and global energy balance. The model has six temperature structure parameters and four molecular abundances, expressed as deviations from thermochemical equilibrium and solar abundances. Recognizing the excess of model parameters over data, our goal is to rule out unreasonable areas of phase space rather than to determine a unique composition and thermal profile. An MCMC routine runs a wide range of inversion and non-inversion models, integrates the resulting spectra against the *Spitzer* bandpasses, and calculates χ^2 against the four data points. Integrals over the MCMC posterior distribution produce robust statistical statements about the unconstrained model.

Figure 12 shows the observed planet–star flux ratios and two model spectra. We find that the observations can be explained by models with and without thermal inversions. We note that the observations are also consistent with a blackbody planetary spectrum with $T = 3200$ K, although a blackbody spectrum is likely unrealistic. An atmosphere can have a blackbody spectrum either if it is isothermal over the upper several optical depths or if there is no opacity source. Neither condition is physically favorable. Several spectrally active molecules should be abundant in hot-Jupiter atmospheres and there is collision-induced opacity (Freedman et al. 2008). In addition to being coupled with the opacities, the temperature structure is also critically influenced by atmospheric dynamics (Showman et al. 2009), all of which can cause a non-isothermal profile.

At 3200 K, the temperature of early M-class stellar photospheres, CO and H₂O are the dominant spectroscopically active molecules in the IR. Other molecules like CH₄ and CO₂ are negligible, under the assumption of thermochemical equilibrium with solar abundances. CO has a strong absorption feature in the 4.5 μm channel. H₂O contributes the dominant opacity in the 5.8 μm channel and contributes significantly in the remaining channels. Thus, for temperature decreasing monotonically with altitude, i.e., in the absence of a thermal inversion, the spectra should exhibit noticeable absorption in the 4.5 and 5.8 μm channels and less in the 3.6 μm and 8 μm channels (Madhusudhan & Seager 2010, 2011). The observed planet–star flux contrast in the 4.5 μm channel should then be lower than that in the 3.6 μm channel (Charbonneau et al. 2008; Stevenson et al. 2010); the difference depends on the temperature gradient and the composition.

Our observations of WASP-18b show excess flux at 4.5 μm , compared to the 3.6 μm channel. This could be due to a thermal

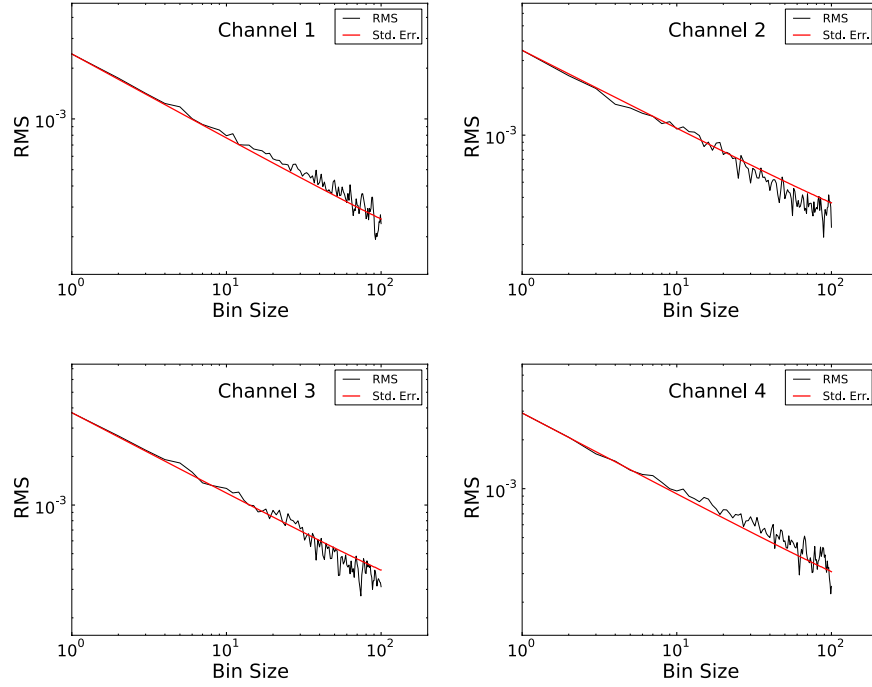


Figure 7. rms residual flux vs. bin size in each channel. This plot tests for correlated noise. The straight line is the prediction for Gaussian white noise. Since the data do not deviate far from the line, the effect of correlated noise is minimal.

(A color version of this figure is available in the online journal.)

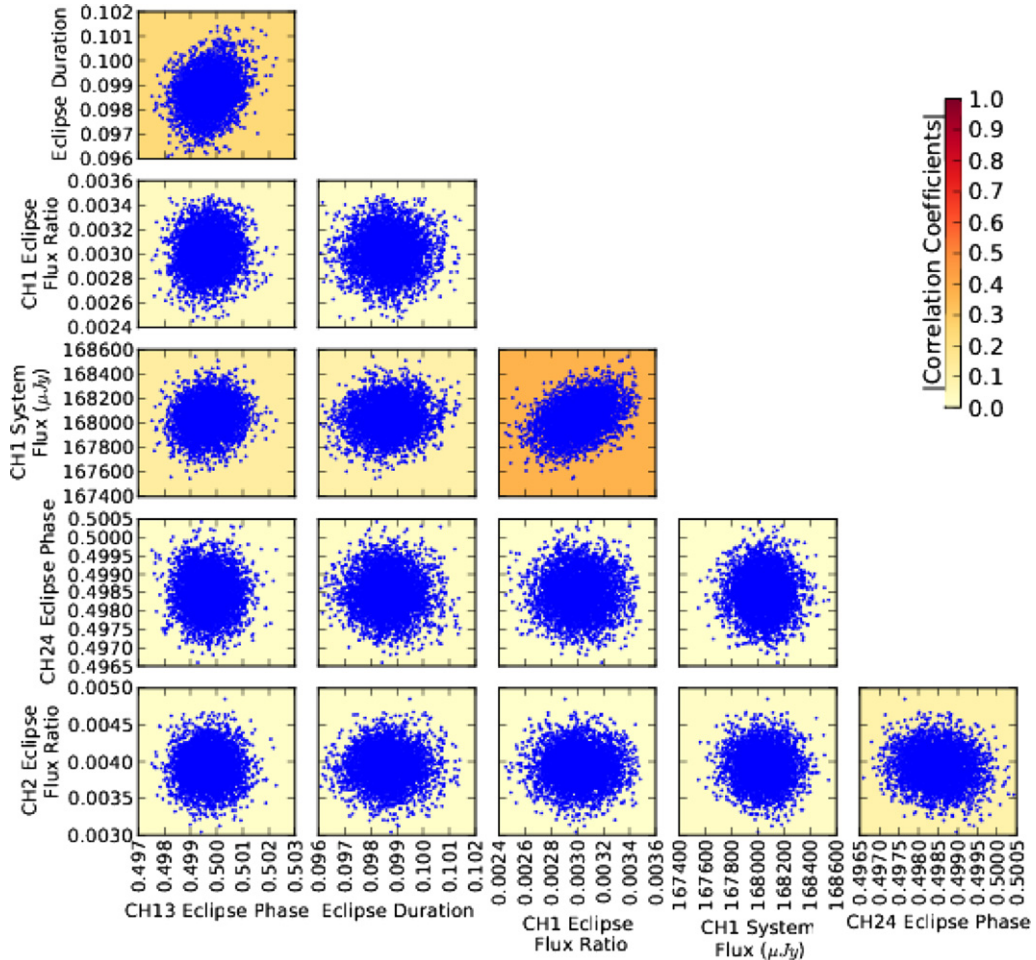


Figure 8. Parameter correlations. To decorrelate the Markov chains and unclutter the plot, one point appears for every 1000th MCMC step. Each panel contains all the points.

(A color version of this figure is available in the online journal.)

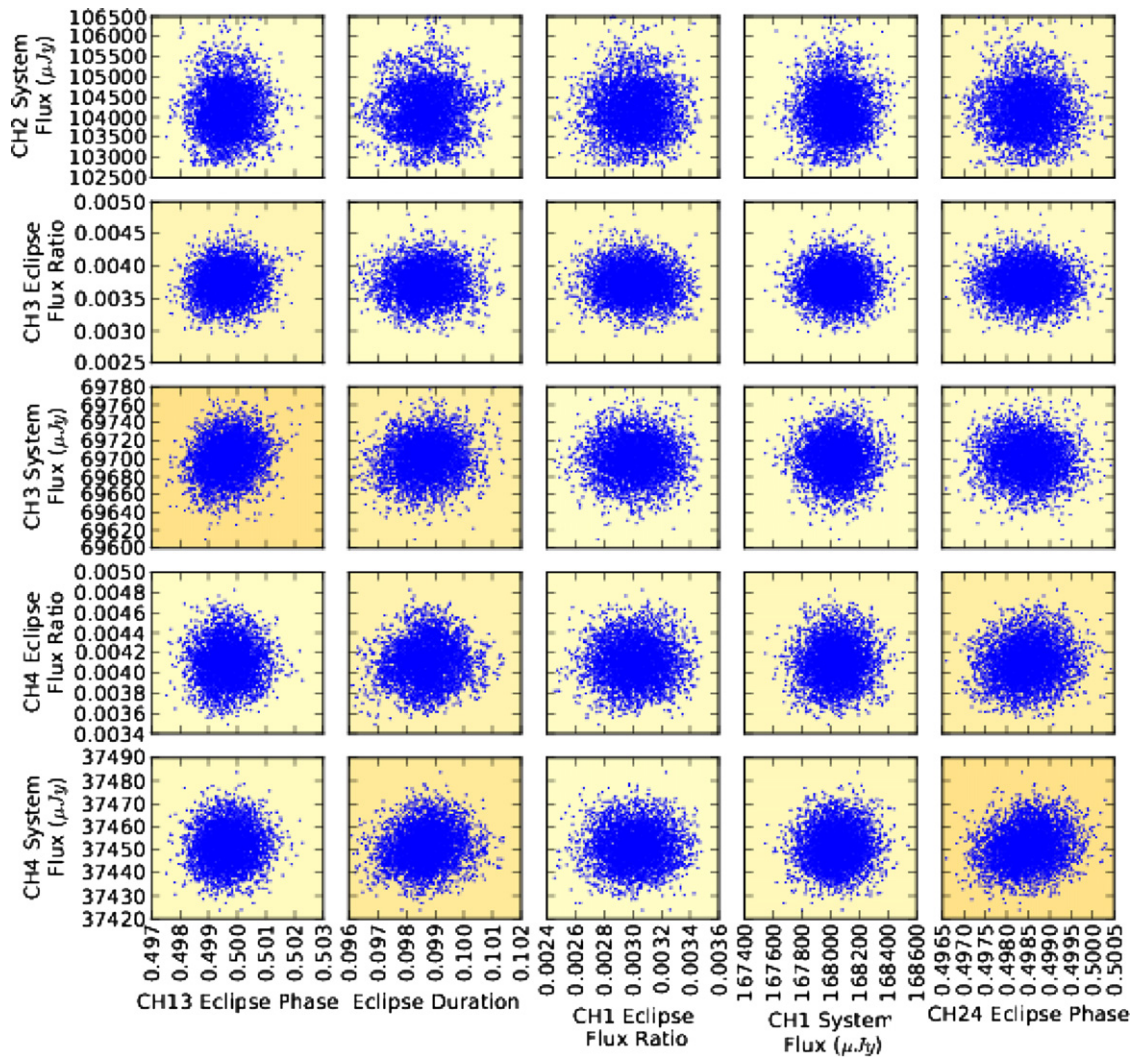


Figure 9. Parameter correlations, continued. Same as Figure 8.

(A color version of this figure is available in the online journal.)

inversion, but the observational uncertainties also allow only a gentle temperature gradient and no inversion, such that the absorption features are not too deep, and a different chemical composition (Madhusudhan & Seager 2010). Two models, with and without an inversion, appear in Figure 12. Both explain the data fairly well, the inversion model at the 1σ level and the non-inversion model within 1.5σ . The molecular abundances of the models are only marginally different from those of thermochemical equilibrium with solar abundances (TE_{\odot}). The inversion model has 10 times more CO, and the non-inversion model has 10 times less H_2O and CO compared to TE_{\odot} . The mixing ratio of CO_2 is 10^{-7} for the inversion model and 10^{-8} for the non-inversion model. Despite the weak constraints on the temperature structure, the observations do place a strict constraint on the day–night energy redistribution in WASP-18b: both models require a low Bond albedo (A) and inefficient day–night redistribution ($\lesssim 0.1$ for $A = 0$) in WASP-18b. Figure 13 shows the contribution functions of the two models in the four IRAC channels, along with the thermal profiles.

The presence of a thermal inversion in the dayside atmosphere of WASP-18b is expected based on theoretical grounds (Hubeny et al. 2003; Fortney et al. 2008). At the high temperatures of this planet, TiO and VO can exist in gas phase over the entire atmosphere, thus contributing to the strong visible opacities

required to form stratospheres. However, questions of whether the concentrations of TiO/VO alone are adequate to cause the required thermal inversion, and whether or not other sources of visible/UV opacity are possible at these temperatures, merit future theoretical investigation (Spiegel et al. 2009; Zahnle et al. 2009a). Furthermore, Knutson et al. (2010) find that the host star WASP-18 has a low activity level, indicating that inversion-causing compounds are not likely to be destroyed by stellar UV radiation, thereby also favoring the presence of a thermal inversion. Thus, WASP-18b is an apt candidate for follow-up observations searching for thermal inversions. Stronger constraints on the temperature structure of WASP-18b are possible in the near future if ground-based observations of thermal emission become available (Madhusudhan et al. 2011). Also, the low day–night energy redistribution required by the present observations can be verified by potential future observations of thermal phase curves (e.g., Knutson et al. 2008) of WASP-18b.

5. ORBITAL DYNAMICS

Our secondary eclipse times further constrain the planet’s already-precise orbital parameters. Triaud et al. (2010) detect an eccentricity for WASP-18b of $e = 0.0085 \pm 0.0008$, the

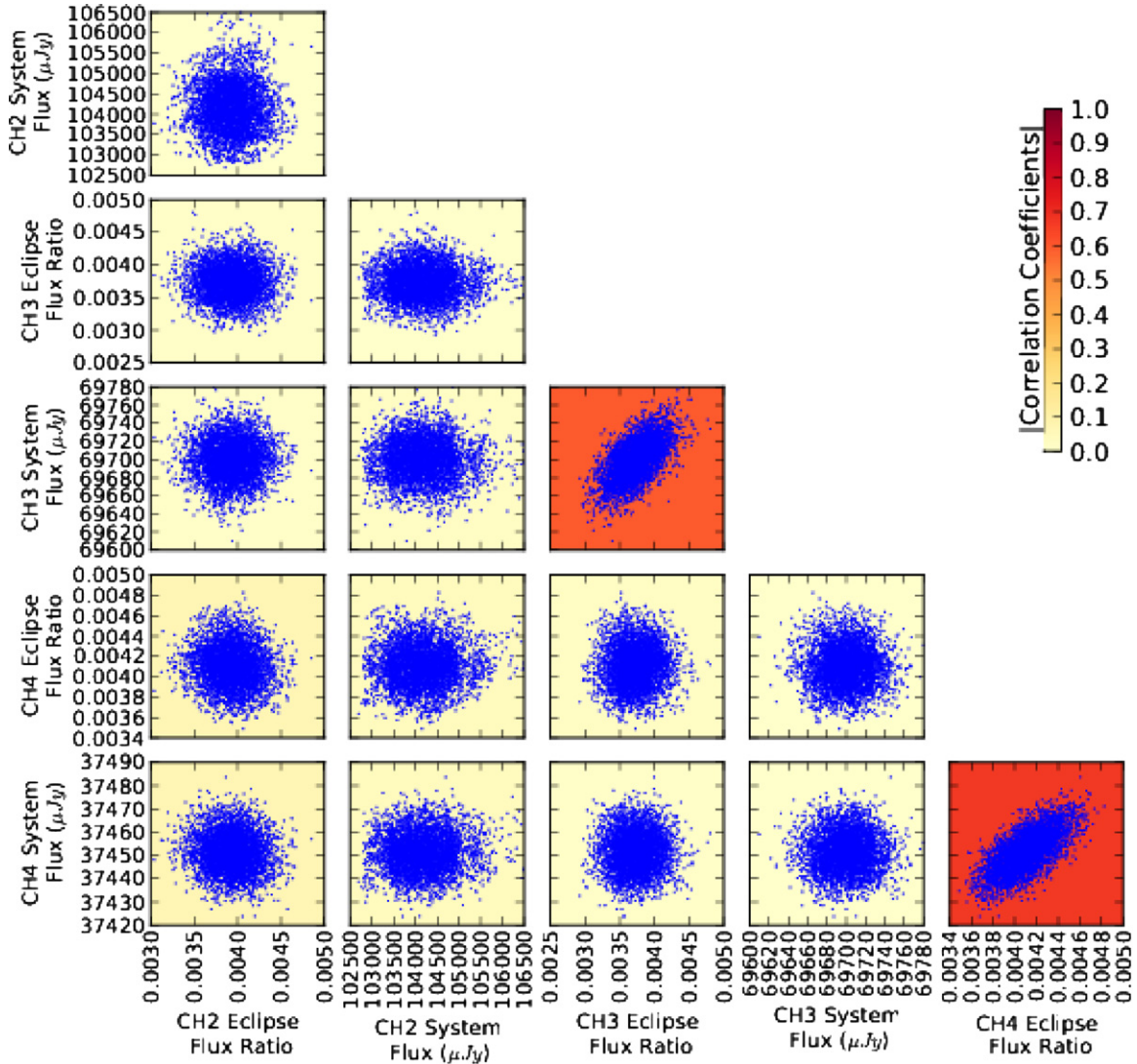


Figure 10. Parameter correlations, continued. Same as Figure 8.

(A color version of this figure is available in the online journal.)

lowest fully determined value for any transiting planet measured with such precision. A joint photometric fit to all four *Spitzer* observations yields a midpoint phase of 0.4990 ± 0.0004 for the Hellier et al. (2009) ephemeris, and a duration of $D_s = 0.0927 \pm 0.0007$ days, which is longer than the transit duration of Hellier et al. (2009) by 4.8σ . By itself, after a 20 s light-time correction, the eclipse midpoint tells us that $e \cos \omega = -0.0016 \pm 0.0007$, where ω is the longitude of periastron. We combine the eclipse phase and duration with known transit parameters from Hellier et al. (2009) to determine that $e \sin \omega = 0.0198 \pm 0.0072$. To do this, we use Equation (18) from Ragozzine & Wolf (2009) as derived by Kopal (1959):

$$e \sin \omega = \left(\frac{D_s - D_p}{D_s + D_p} \right) \left(\frac{\alpha^2 - \cos^2 i}{\alpha^2 - 2 \cos^2 i} \right). \quad (8)$$

D_p is the transit duration and D_s is the secondary eclipse duration. We define $\alpha = (R_*/a)(1 + R_p/R_*)(1/\sqrt{1 - e^2})$ and $\cos i = b_p(R_*/a)(1 + e \sin \omega / (1 - e^2))$, and $R_*/a = (D_p/P)(\pi/\sqrt{(R_p/R_*)^2 - b_p^2})$, where R_p and R_* are the planetary and stellar radii, respectively, a is the orbit's semimajor axis, P is the orbital period, and b_p is the impact parameter in units of the

stellar radius. We solved the equation numerically for $e \sin \omega$, and the uncertainties come from sampling Gaussian distributions generated from the uncertainties of the input parameters.

We jointly fit an MCMC orbit model (Campo et al. 2011) to the BJD time for 2 eclipses, 37 RV data points from Triaud et al. (2010), and 6 transit midpoints extracted from the photometry of Southworth et al. (2009), omitting 3 RV points subject to the Rossiter–McLaughlin effect. This results in a total of 45 data points, 42 of which are included. Our model has six free parameters. Results are given in Table 3, where T_0 is the ephemeris time, K is the RV amplitude, and γ is the barycentric velocity.

We find from the fit above that $e \cos \omega = -0.00014 \pm 0.00053$, consistent with 0, leaving e dominated by its $e \sin \omega$ component. We note that the value of $e \sin \omega$ found photometrically is positive, while the value in our joint fit is negative. Eclipse timing does not effectively constrain $e \sin \omega$. RV measurements have a known tendency to overestimate e when it is low (Laughlin et al. 2005). A key sign of this is a value of $\omega \sim \pm 90^\circ$. Photometric information, such as the measured durations for our eclipses, cannot yet independently confirm a non-zero $e \sin \omega$ beyond the 3σ level. Precise determination of e is important because the circularization timescale for a tidal

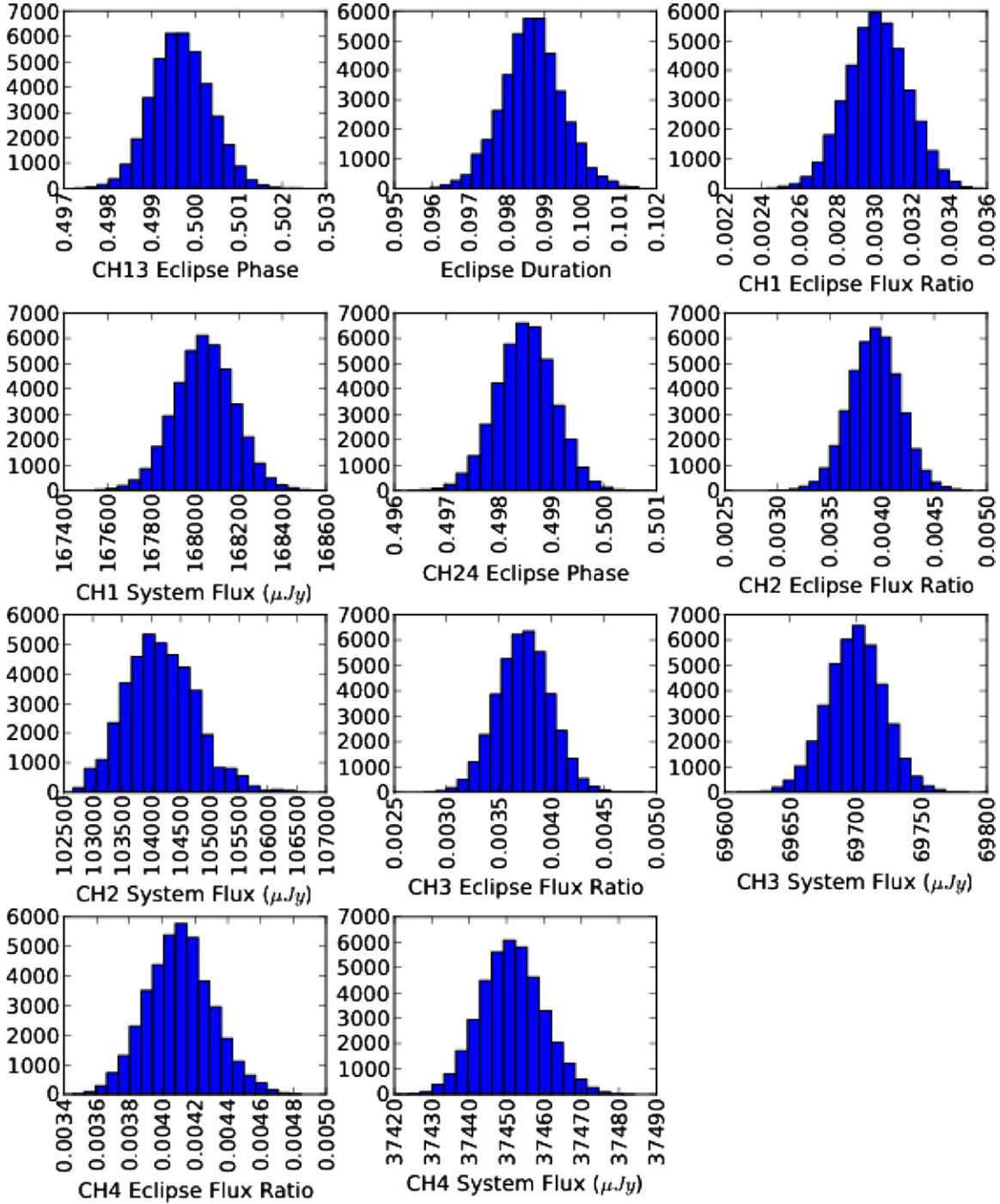


Figure 11. Parameter histograms. To decorrelate the Markov chains, the histograms come from every 100th MCMC step.
(A color version of this figure is available in the online journal.)

damping quality factor, $Q_p \sim 10^6$ (Mardling 2007), is comparable to the age of the system. Whether the orbit is still eccentric determines if it is still experiencing tidal dissipation, which drives the evolution of the system. We perform a comparison fit with $e = 0$, but its BIC value of 155 is considerably higher than BIC = 102 for the eccentric fit.

To determine if the eccentricity we found could have come up by random chance, we also performed an experiment similar to that of Laughlin et al. (2005) in which we generated 10^5 RV data sets for a planet in a circular orbit with the same period, mid-transit time, and semi-amplitude as our best fit for

WASP-18b. In each data set, the BJD of each observation was kept the same as in the real WASP-18b data set. We added Gaussian noise corresponding to the instrumental error for each observation and a 3 m s^{-1} stellar jitter consistent with the tables of Wright (2005), in quadrature. We retained the transit and eclipse timings. We then used a minimizer to find combinations of $e \sin \omega$ and $e \cos \omega$ that minimize the χ^2 corresponding to each data set. The mean and standard deviation of $e \sin \omega$ and $e \cos \omega$ were 0.0000 ± 0.0012 and -0.0003 ± 0.0002 , respectively. The 3σ upper limit on $|e \sin \omega|$ is 0.0036, well below our best-fit value in the real data set. This is not surprising because of the

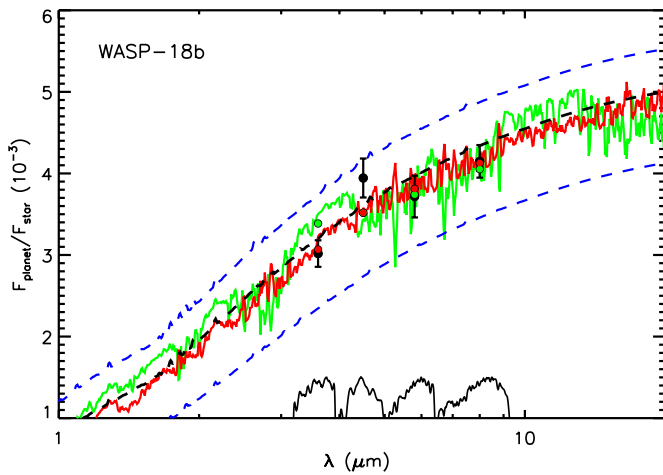


Figure 12. Dayside spectrum of WASP-18b. The black circles with error bars show our observations of WASP-18b in the four *Spitzer*/IRAC channels. The red curve shows the inversion model spectrum and the green curve shows the non-inversion model spectrum discussed in the text. The red and green circles are the respective spectra integrated over the *Spitzer* bandpasses (indicated with an arbitrary scale at the bottom). The black dashed line shows a blackbody at 3150 K, and the blue dashed lines show blackbody spectra corresponding to the minimum and maximum temperatures in the atmosphere (see Figure 13).

(A color version of this figure is available in the online journal.)

high signal-to-noise ratio and even sampling (Triaud et al. 2010) of the RV data ($K/(\sigma_{RV}) \sim 180$). Given the MCMC results, the BIC comparison between the fits to a circular and non-circular orbit, the Monte Carlo experiments, and the weak but consistent photometric support, and despite the improbable orientation of the orbit, the 7σ non-zero eccentricity of WASP-18b's orbit is likely not an overestimate.

Despite WASP-18b's short period and close proximity to its host star, its high density and low eccentricity make it a poor candidate for the detection of apsidal precession (Ragozzine & Wolf 2009; Campo et al. 2011). The precession should manifest itself as an eclipse/transit timing variation with a period of 600 years and an amplitude of $(eP)/\pi$, or about 4 minutes (Ragozzine & Wolf 2009). Given the orbit's current orientation, apsidal motion could be detectable as an ~ 7 ms difference

Table 3
Joint Orbital Fits

Parameter	Value
$e \sin \omega$	0.0091 ± 0.0012
$e \cos \omega$	-0.00014 ± 0.00053
e	0.0091 ± 0.0012
ω ($^\circ$)	-91 ± 3
P (days)	0.9414518 ± 0.0000004
T_0 (MJD) ^a	1084.79363 ± 0.00011
K (m s $^{-1}$)	1818 ± 3
γ (m s $^{-1}$)	3327 ± 2
BIC	102.0

Note. ^a MJD = BJD - 2,454,000 (terrestrial time).

between the best-fit transit and eclipse periods (Giménez & Bastero 1995). This signal would likely be overwhelmed by the modulation of the period due to tidal infall (Hellier et al. 2009), which could be measurable within a few decades. The Applegate effect makes very small transit timing variations unmeasurable (Watson & Marsh 2010). Based on the MCMC results, the BIC comparison between the fits to a circular and non-circular orbit, the Monte Carlo experiments, and the weak but consistent photometric support, we see what appears to be a 7σ , non-zero eccentricity at $\omega = -90^\circ$. Numerous planets with small, albeit significant, eccentricities appear to have $\omega = \pm 90^\circ$ (Campo et al. 2011; Stevenson et al. 2010), raising the question of non-orbital effects that mimic eccentricity. At least one such effect, the influence on radial velocity measurements of stellar tides raised by the planet (Arras et al. 2011) provides an alternative to an eccentric orbit with this improbable orientation.

6. CONCLUSIONS

Spitzer observed two secondary eclipses of WASP-18b using all four channels of the IRAC instrument. A blackbody model fits the observed brightness temperatures relatively well. Slightly better fits to both inversion and non-inversion models exist with the inversion model somewhat preferred. Because the planet is so much brighter than its predicted equilibrium

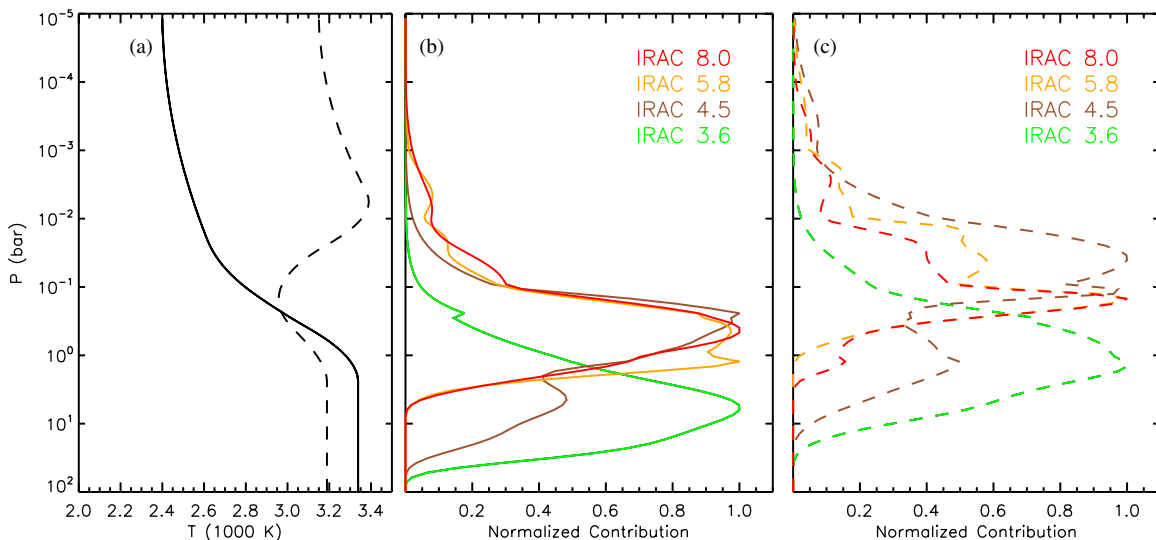


Figure 13. Pressure-temperature profile (left) and contribution functions (middle and right). The middle and right panels show the normalized contribution functions for the non-inversion and inversion models, respectively, in the indicated *Spitzer* filters, with wavelengths in μm . The left panel overlays the profiles for both models.

(A color version of this figure is available in the online journal.)

temperature for uniform redistribution, the model requires near-zero albedo and very low day–night energy redistribution. The very small scale height makes this atmosphere interesting as an extreme example among irradiated planets. The addition of secondary eclipse data also improves the orbital parameters, confirming a slight eccentricity. Files containing the light curves, model fits, source centers, and other ancillary data appear in the online journal.

We thank Drake Deming for helpful discussions. We received free software and services from SciPy, Matplotlib, and the Python Programming Language community; W. Landsman and other contributors to the Interactive Data Language Astronomy Library, the free and open-source software communities; the NASA Astrophysics Data System; and the JPL Solar System Dynamics group. This work is based in part on observations made with the *Spitzer Space Telescope*, which is operated by the Jet Propulsion Laboratory, California Institute of Technology, under a contract with NASA. Support for this work was provided by NASA through an award issued by JPL/Caltech.

REFERENCES

- Arras, P., Burkart, J., Quataert, E., & Weinert, N. N. 2011, *MNRAS*, submitted (arXiv:1107.6005)
- Beaulieu, J.-P., Tinetti, G., Kipping, D. M., et al. 2011, *ApJ*, **731**, 16
- Burrows, A., Ibgui, L., & Hubeny, I. 2008, *ApJ*, **682**, 1277
- Campo, C. J., Harrington, J., Hardy, R. A., et al. 2011, *ApJ*, **727**, 125
- Charbonneau, D., Allen, L. E., Megeath, S. T., et al. 2005, *ApJ*, **626**, 523
- Charbonneau, D., Knutson, H. A., Barman, T., et al. 2008, *ApJ*, **686**, 1341
- Deming, D., Seager, S., Richardson, L. J., & Harrington, J. 2005, *Nature*, **434**, 740
- Fazio, G. G., Hora, J. L., Allen, L. E., et al. 2004, *ApJS*, **154**, 10
- Fortney, J. J., Lodders, K., Marley, M. S., & Freedman, R. S. 2008, *ApJ*, **678**, 1419
- Freedman, R. S., Marley, M. S., & Lodders, K. 2008, *ApJS*, **174**, 504
- Giménez, A., & Bastero, M. 1995, *Ap&SS*, **226**, 99
- Harrington, J., Luszcz, S. H., Seager, S., Deming, D., & Richardson, L. J. 2007, *Nature*, **447**, 691
- Hellier, C., Anderson, D. R., Collier Cameron, A., et al. 2009, *Nature*, **460**, 1098
- Hubeny, I., Burrows, A., & Sudarsky, D. 2003, *ApJ*, **594**, 1011
- Knutson, H. A., Charbonneau, D., Allen, L. E., Burrows, A., & Megeath, S. T. 2008, *ApJ*, **673**, 526
- Knutson, H. A., Charbonneau, D., Burrows, A., O'Donovan, F. T., & Mandushev, G. 2009a, *ApJ*, **691**, 866
- Knutson, H. A., Charbonneau, D., Cowan, N. B., et al. 2009b, *ApJ*, **703**, 769
- Knutson, H. A., Howard, A. W., & Isaacson, H. 2010, *ApJ*, **720**, 1569
- Kopal, Z. 1959, *Close Binary Systems* (The International Astrophysics Series; London: Chapman and Hall)
- Laughlin, G., Marcy, G. W., Vogt, S. S., Fischer, D. A., & Butler, R. P. 2005, *ApJ*, **629**, L121
- Liddle, A. R. 2007, *MNRAS*, **377**, L74
- Machalek, P., McCullough, P. R., Burke, C. J., et al. 2008, *ApJ*, **684**, 1427
- Machalek, P., McCullough, P. R., Burrows, A., et al. 2009, *ApJ*, **701**, 514
- Machalek, P., et al. 2011, *ApJ*, submitted
- Madhusudhan, N., Harrington, J., Stevenson, K. B., et al. 2011, *Nature*, **469**, 64
- Madhusudhan, N., & Seager, S. 2009, *ApJ*, **707**, 24
- Madhusudhan, N., & Seager, S. 2010, *ApJ*, **725**, 261
- Madhusudhan, N., & Seager, S. 2011, *ApJ*, **729**, 41
- Mandel, K., & Agol, E. 2002, *ApJ*, **580**, L171
- Mardling, R. A. 2007, *MNRAS*, **382**, 1768
- O'Donovan, F. T., Charbonneau, D., Harrington, J., et al. 2010, *ApJ*, **710**, 1551
- Pont, F., Zucker, S., & Queloz, D. 2006, *MNRAS*, **373**, 231
- Ragozzine, D., & Wolf, A. S. 2009, *ApJ*, **698**, 1778
- Seager, S., & Mallén-Ornelas, G. 2003, *ApJ*, **585**, 1038
- Showman, A. P., Fortney, J. J., Lian, Y., et al. 2009, *ApJ*, **699**, 564
- Sing, D. K., & López-Morales, M. 2009, *A&A*, **493**, L31
- Southworth, J., Hinse, T. C., Dominik, M., et al. 2009, *ApJ*, **707**, 167
- Southworth, J., Wheatley, P. J., & Sams, G. 2007, *MNRAS*, **379**, L11
- Spiegel, D. S., Silverio, K., & Burrows, A. 2009, *ApJ*, **699**, 1487
- Stevenson, K. B., Harrington, J., Nymeyer, S., et al. 2010, *Nature*, **464**, 1161
- TriAUD, A. H. M. J., Collier Cameron, A., Queloz, D., et al. 2010, *A&A*, **524**, A25
- Watson, C. A., & Marsh, T. R. 2010, *MNRAS*, **408**, 601
- Wheatley, P. J., Collier Cameron, A., Harrington, J., et al. 2011, *ApJ*, submitted (arXiv:1004.0836)
- Winn, J. N., Holman, M. J., Torres, G., et al. 2008, *ApJ*, **683**, 1076
- Wright, J. T. 2005, *PASP*, **117**, 657
- Zahnle, K., Marley, M. S., & Fortney, J. J. 2009a, *ApJ*, submitted (arXiv:0911.0728)
- Zahnle, K., Marley, M. S., Freedman, R. S., Lodders, K., & Fortney, J. J. 2009b, *ApJ*, **701**, L20